Wave Motion 65 (2016) 156–174

Contents lists available at ScienceDirect

Wave Motion

journal homepage: www.elsevier.com/locate/wavemoti

A Whitham–Boussinesq long-wave model for variable topography

R.M. Vargas-Magaña *, P. Panayotaros

Departamento de Matemáticas y Mecánica IIMAS, Universidad Nacional Autónoma de México, Apdo. Postal 20-726, 01000 México D.F., México

HIGHLIGHTS

- Present bidirectional nonlocal shallow water wave model for variable depth.
- Nonlocality introduced through simplified variable depth Dirichlet–Neumann operator.
- Study variable depth effects in linear normal modes, examples of steepening and modulation.
- Show qualitative agreement with some higher order constant depth nonlocal models.
- Model exhibits combination of nonlinear and variable depth effects.

ARTICLE INFO

Article history:
Received 7 January 2016
Received in revised form 27 March 2016
Accepted 26 April 2016
Available online 11 May 2016

Keywords:
Shallow water wave theory
Variable bottom topography
Whitham–Boussinesq model
Hamiltonian system
Dirichlet–Neumann operator
Pseudo-differential operator

ABSTRACT

We study the propagation of water waves in a channel of variable depth using the long-wave asymptotic regime. We use the Hamiltonian formulation of the problem in which the non-local Dirichlet–Neumann operator appears explicitly in the Hamiltonian, and propose a Hamiltonian model for bidirectional wave propagation in shallow water that involves pseudo-differential operators that simplify the variable-depth Dirichlet–Neumann operator. The model generalizes the Boussinesq system, as it includes the exact dispersion relation in the case of constant depth. Analogous models were proposed by Whitham for unidirectional wave propagation. We first present results for the normal modes and eigenfrequencies of the linearized problem. We see that variable depth introduces effects such as a steepening of the normal modes with the increase in depth variation, and a modulation of the normal mode amplitude. Numerical integration also suggests that the constant depth nonlocal Boussinesq model can capture qualitative features of the evolution obtained with higher order approximations of the Dirichlet–Neumann operator. In the case of variable depth we observe that wave-crests have variable speeds that depend on the depth. We also study the evolutions of Stokes waves initial conditions and observe certain oscillations in width of the crest and also some interesting textures and details in the evolution of wave-crests during the passage over obstacles.

© 2016 Elsevier B.V. All rights reserved.

1. Introduction

The precise description of the propagation of water waves on the surface of a body of water is an issue of great interest in physics and mathematics. Since the nineteenth century when d'Alembert, Euler, Lagrange and Bernoulli established the system of equations governing the motion of surface waves of an irrotational ideal fluid under the effect of gravity, different

* Corresponding author.
E-mail addresses: rmvargas@ciencias.unam.mx (R.M. Vargas-Magaña), panos@mym.iimas.unam.mx (P. Panayotaros).

http://dx.doi.org/10.1016/j.wavemoti.2016.04.013
0165-2125/© 2016 Elsevier B.V. All rights reserved.

scientists and engineers have turned to the derivation of simplified models that have often led to good approximations to the water wave problem in different physical regimes.

Moreover due to its importance to coastal engineering, water wave propagation in variable depth has become a prolific topic of research. There is a large literature on the subject, and we can cite in particular articles of Johnson [1], Whitham [2], Miles [3], Nachbin and Papanicolaou [4], van Groesen and Pudjaprasetya [5], Yoon Liu [6] and Kirby [7].

One of the biggest difficulties that arise when attempting to solve the equations is that they constitute a free boundary problem. For the case of 2D-water waves where the surface evolves as a function of one spatial variable and time, there are several techniques that can be used to eliminate the vertical spatial coordinate and to reduce the problem to the evolution of wave height and the evolution of the velocity potential on the free surface. Methods that have been effective in the 2D problem include conformal mapping and singular integral equations, see A. Nachbin and G. Papanicolaou [4], B. Fornberg [8], J. Dold [9], Zakharov [10], Radder [11].

The Hamiltonian formulation of the water wave problem is due to Zakharov [10], see also works of Radder [11], and Miles [12]. V. Zakharov pointed out that the water wave problem can be restated as a Hamiltonian system in terms of surface quantities, the wave amplitude and the surface hydrodynamic potential. This formulation was developed further by Craig and Sulem, who introduced the Dirichlet–Neumann operator explicitly, and approximated it systematically by small wave amplitude expansions, see, [13]. Analogous expressions for the Dirichlet–Neumann operator in variable depth were derived by Craig, Guyenne, Nicholls and Sulem in [14], where the authors also present expansions of the linear (i.e. flat surface) Dirichlet–Neumann operator in the depth variation. Assuming the validity of the small amplitude expansion, the Dirichlet–Neumann operator for arbitrary wave amplitude is computed recursively in terms of the linear Dirichlet–Neumann operator for arbitrary bottom topography.

In this work we propose a non-local Hamiltonian model for bidirectional wave propagation in shallow water that involves pseudo-differential operators that simplify the linear Dirichlet–Neumann operator for variable depth. The starting point is the general variable depth theory of [14], and its simplification to a Boussinesq-type equation for long waves, and small depth variations in [15]. In [15] the constant depth component of the linear part is also replaced by the exact dispersive term, leading to a bidirectional analogue of the Whitham equation, see also [16]. Constant depth Whitham equations have received significant attention recently, see [17], and there are results suggesting that the weaker dispersion leads to more realistic behavior at higher amplitudes. The bidirectional Whitham–Boussinesq versions also avoid the ill-posedness of the linear Boussinesq system. In [15] it was also seen that the lowest order variable depth correction to the Dirichlet–Neumann operator generally results in topography effects that are likely unreasonably weak. To obtain better results one may consider more complicated expressions for the linear Dirichlet–Neumann operator, such as higher order expansions in the depth variation, see Guyenne and Nicholls [18,19] and Gouin et al. [20] for a recent implementation, [14] for additional semi-explicit expressions.

Instead, we here use an operator that has a relatively simple expression and satisfies some structural properties of the exact linear Dirichlet–Neumann operator $G_0(\beta)$, β the function describing the depth. The operator $\mathcal{A}_{G_0} = \text{Approximate}(G_0(\beta))$ we are proposing is $\mathcal{A}_{G_0} = \text{sym}(D\tanh(h(x)D))$. The corresponding Whitham–Boussinesq system is defined in Section 2. This is clearly an *ad-hoc* simplification of the linear Dirichlet–Neumann operator, but it is simple enough, and reduces to the exact constant depth expression. In Section 3 we discuss some general structural properties to require for the operator $\mathcal{A}_{G_0}$, such as symmetry, positivity, and the high wavelength asymptotics of the constant depth operator. These are either checked directly or verified numerically in Section 3.

The numerical spectral analysis of the matrix obtained from the model linear Dirichlet–Neumann operator $\mathcal{A}_{G_0}$ for different (periodic) depth profiles shows significant effects of the topography on the normal modes. These include steepening of the normal mode profile in the lowest and medium frequency range, and amplitude modulation that follows the topography. This is seen in the intermediate frequency modes.

Numerical integration of the Whitham–Boussinesq system with constant depth shows some qualitative similarity with the evolution obtained by [21] using higher order amplitude terms in the Dirichlet–Neumann operator. In the variable depth case we see that the speed of wave-crests follows changes in the depth. Also we see an example of how this effect alters the shape of Stokes wavetrains.

The model includes variable topography effects and seems simple enough to motivate further theoretical study. Its validation requires comparisons with more accurate models, e.g. ones using a more precise computation of $G_0(\beta)$. We hope to pursue some of these problems in future work.

The organization of this paper is as follows. In Section 2 we present the Hamiltonian formulation of the water wave problem and propose the Whitham–Boussinesq model for variable depth. In Section 3 we discuss some general ideas for simplifying the Dirichlet–Neumann operator and present a numerical spectral analysis of the particular choice we use for different depth profiles. In Section 4 we present numerical simulations of the Whitham–Boussinesq equations with constant and variable depths.

2. Hamiltonian formulation of the free surface problem and Whitham–Boussinesq models

We consider an ideal fluid, *i.e.* incompressible and inviscid, where the flow is assumed to be irrotational and surface tension is neglected. The fluid occupies a two dimensional time-dependent simply connected domain $\mathcal{D}_t$, given by

$$\mathcal{D}_t(\beta,\eta) := \{(x,y) : x \in \mathbb{R},\ -h_0 + \beta(x) < y < \eta(x,t)\},$$

whose boundary is given by

$$\partial \mathcal{D}_t(\beta, \eta) := \{(x, y) : y = \eta(x, t) \text{ and } y = -h_0 + \beta(x)\}, \tag{2.1}$$

where h_0 is the mean depth, $\beta(x)$ is the variation of the depth from this value, and η measures the perturbation of the free surface of the fluid from $y = 0$. We assume $\beta(x) < h_0$ for every $x \in \mathbb{R}$.

We also assume that the only bulk force acting on the fluid mass is gravity and that the pressure p at the free surface fluid is constant, $p = 0$. The Euler equations for free surface potential flow is then

$$\Delta\varphi(x, y) = 0 \quad \text{in } D_t(\beta, \eta), \tag{2.2}$$

$$\partial_t \eta = \partial_y \varphi - (\partial_x \eta)(\partial_x \varphi) \quad \text{in } y = \eta(x, t) \tag{2.3}$$

$$\partial_t \varphi = -\frac{1}{2}|\nabla\varphi|^2 - g\eta \quad \text{in } y = \eta(x, t) \tag{2.4}$$

$$\nabla\varphi \cdot N(\beta) = 0 \quad \text{in } y = -h_0 + \beta(x), \tag{2.5}$$

where φ is the velocity potential and the velocity is given by $u = \nabla\varphi$. $g > 0$ is the gravitational constant. Moreover $N(\beta)$ is the exterior unit normal on the rigid boundary.

The spatially periodic version of the above equation assumes boundary conditions $\eta(x+L, t) = \eta(x, t)$ and $\varphi(x+L, y, t) = \varphi(x, y, t)$ for some period $L > 0$. The periodic version will be used in the numerical simulations below.

V. Zakharov [10] showed that the water wave problem (2.2)–(2.5) can be restated as a Hamiltonian system with infinitely many degrees of freedom in terms of surface quantities, the wave amplitude $\eta(x, t)$ and surface potential $\xi(x, t) = \varphi(x, \eta(x, t), t)$, namely as

$$\partial_t \begin{pmatrix} \eta \\ \xi \end{pmatrix} = \begin{pmatrix} 0 & I \\ -I & 0 \end{pmatrix} \begin{pmatrix} \dfrac{\delta H}{\delta \eta} \\ \dfrac{\delta H}{\delta \xi} \end{pmatrix}. \tag{2.6}$$

The Hamiltonian can be expressed explicitly in terms of η and ξ as

$$H = \frac{1}{2}\int_{\mathbb{R}} (\xi G(\beta, \eta)\xi + g\eta^2) dx, \tag{2.7}$$

see [13], where the operator $G(\beta, \eta)$ is defined as follows: consider the elliptic problem

$$\Delta\varphi(x, y) = 0, \quad \forall\, (x, y) \in D_t\eta, \tag{2.8}$$

$$\varphi(x, \eta(x)) = \xi(x), \quad \forall\, x \in \mathbb{R}, \tag{2.9}$$

$$\frac{\partial\varphi}{\partial\hat{n}}(x, -h_0 + \beta(x)) = 0, \quad \forall\, x \in \mathbb{R}. \tag{2.10}$$

If η and ξ are sufficiently smooth and decay at infinity then (2.8)–(2.10) admits a unique solution and we can compute the normal derivative of the solution at the surface $y = \eta$. The Dirichlet–Neumann operator $G(\beta, \eta)$ is then defined by

$$(G(\beta, \eta)\xi)(x) = (1 + (\partial_x\eta(x))^2)^{\frac{1}{2}} \nabla\varphi(x, \eta(x)) \cdot N(\eta(x)), \tag{2.11}$$

where $N(\eta(x)) = (1 + (\partial_x\eta(x))^2)^{-\frac{1}{2}}(-\partial_x\eta(x), 1), x \in \mathbb{R}$, is the exterior unit normal at the free surface. The Dirichlet–Neumann operator $G(\beta, \eta)$ is a linear operator on ξ and is symmetric. A similar definition applies to the periodic problem.

In [14], Craig, Guyenne, Nicholls and Sulem give an expansion of this operator in the presence of non-trivial bottom topography

$$G(\beta, \eta) = G_0(\beta, \eta) + G_1(\beta, \eta) + G_2(\beta, \eta) + \cdots, \tag{2.12}$$

where the G_j are homogeneous of degree j in η. The first terms are

$$G_0(\beta, \eta) = D\tanh(h_0 D) + DL(\beta), \tag{2.13}$$

$$G_1(\beta, \eta) = D\eta D - G_0\eta G_0, \tag{2.14}$$

$$G_2(\beta, \eta) = \frac{1}{2}(G_0 D\eta^2 D - D^2\eta^2 G_0 - 2G_0\eta G_1), \tag{2.15}$$

where $D = -i\partial_x$. The operators G_j involve formal pseudo-differential operators of the form

$$a(x, D)\xi(x) = \int_{\mathbb{R}} a(x, k)\hat{\xi}(k)e^{ikx} dk. \tag{2.16}$$

where the function $a(x, k)$ is the *symbol* of $a(x, D)$.

At higher order, the G_j, $j > 2$, are similarly obtained from G_0, using a recursion formula. The recursion formula for the G_j is the one obtained for a flat bottom, where $G_0(0, \eta) = D\tanh(h_0 D)$, see [13]. Variable depth effects are thus encoded in the pseudo-differential operator $L(\beta)$.

The operator $L(\beta)$ acting on the boundary data $\xi(x)$, can be written in the semi-explicit form, see [14]

$$L(\beta) = -B(\beta)A(\beta), \tag{2.17}$$

where the operators $A(\beta)$ and $C(\beta)$ are defined by

$$A(\beta)\xi = \int_{\mathbb{R}} e^{ikx}\sinh(\beta(x)k)\,\mathrm{sech}(hk)\hat{\xi}(k)dk, \tag{2.18}$$

$$C(\beta)\xi = \int_{\mathbb{R}} e^{ikx}\cosh((-h_0+\beta(x))k)\hat{\xi}(k)dk, \tag{2.19}$$

and $B(\beta) = C(\beta)^{-1}$. The inverse $B(\beta)$ of the operator $C(\beta)$ is well defined, see Craig, et al. in [14].

An alternative expression for $L(\beta)$ is in powers of the depth variation β as $L(\beta) = \Sigma_{j=0}^{\infty} L_j(\beta)$, where the $L_j(\beta)$ are homogeneous of order j in β, and are computed recursively, see [14]. The first two terms in the expansion are

$$L_0(\beta) = 0, \tag{2.20}$$

$$L_1(\beta) = -\,\mathrm{sech}(h_0 D)\beta D\,\mathrm{sech}(h_0 D). \tag{2.21}$$

2.1. Long-wave approximations of the operator $G(\beta, \eta)$

We now consider different approximations of the operator $G(\beta, \eta)$ in the Hamiltonian (2.7) and obtain different Hamiltonian shallow water waves models.

(i) Assuming constant depth, $\beta \equiv 0$, we consider the operator G_0 in its exact form and we add the long wave approximation for G_1 considering $O(\epsilon) \sim O(\delta)$, where $\epsilon = \frac{\eta}{h_0}$ and $\delta = \frac{h_0^2}{l^2}$, with l the typical wavelength. We then obtain a modification of the classical Boussinesq scaling regime, see [2],

$$G_{Aprox_0} = \frac{\tilde{D}}{\sqrt{\epsilon}}\tanh\left(h_0\sqrt{\epsilon}\tilde{D}\right) + \epsilon\tilde{D}\tilde{\eta}\tilde{D}, \tag{2.22}$$

where $\tilde{D} = \frac{1}{l}D$ and $\tilde{\eta} = \frac{\eta}{a}$. We may call the resulting equation a "Whitham–Boussinesq" model.

(ii) Assuming smooth and small depth variations, *i.e.* $\beta \sim O(\epsilon)$, it is possible to use an explicit expression of the $L(\beta)$ operator as an expansion in powers of β, see [14]. The long-wave limit uses (2.21),

$$\mathrm{sech}(h_0 D) = 1 - \frac{(h_0 D)^2}{2} + \cdots,$$

and we derive

$$\frac{h_0}{\delta}\tilde{D}L(\tilde{\beta}) = -h_0\tilde{D}\tilde{\beta}\tilde{D} + O(\gamma^2), \tag{2.23}$$

with $\gamma = \frac{\beta}{h_0}$.

Then we add the long-wave approximation of G_1 described above, see [15]:

$$G_{Aprox_1} = \frac{\tilde{D}}{\sqrt{\epsilon}}\tanh\left(\sqrt{\epsilon}\tilde{D}\right) - \tilde{D}\tilde{\beta}\tilde{D} + \epsilon\tilde{D}\tilde{\eta}\tilde{D}, \tag{2.24}$$

with $\tilde{\beta} = \frac{\beta}{h_0}$, assuming $\gamma \sim \beta \sim \epsilon$. This model was studied in [15].

Another option is to approximate numerically (2.17)–(2.19), this direction seems to require some care due to the apparent cancellations of the exponentially increasing and decreasing symbols in the product of (2.17). We hope to examine this in future work.

(iii) Assuming depth variations of order bigger than $O(\epsilon)$, we introduce a pseudo-differential operator with a functional form that is similar to G_0 and takes into account the explicit function $\beta(x)$, and again use long-wave approximation of G_1 above. In particular, we propose

$$G_{Aprox_2} = Sym\left(\frac{\tilde{D}}{\sqrt{\epsilon}}\tanh\left(\sqrt{\epsilon}(1-\beta(x))\tilde{D}\right)\right) + \epsilon\tilde{D}\tilde{\eta}\tilde{D}, \tag{2.25}$$

where $-1 + \tilde{\beta}(x)$ is the vertical coordinate of the bottom, and *Sym* refers to the symmetrized operator, discussed in more detail in the next section. The linear part reduces to that of the Whitham–Boussinesq equation of (2.22) for $\beta \equiv 0$.

The Hamiltonians arising from using G_{Aprox_0}, G_{Aprox_1}, and G_{Aprox_2} in (2.7) will be denoted by H_0, H_1, and H_2 respectively. For instance

$$H_2 = \frac{1}{2}\int_{\mathbb{R}} \left[\xi^* \left(Sym\left(\frac{\tilde{D}}{\sqrt{\epsilon}} \tanh\left(\sqrt{\epsilon} h(x^*) \tilde{D} \right) \right) + \epsilon \tilde{D} \tilde{\eta} \tilde{D} \right) \xi^* + \eta^{*2} \right] dx^*, \tag{2.26}$$

where $\xi^* = \frac{\xi}{\epsilon c_0 l}$, $x^* = \frac{x}{l}$ and $\eta^* = \frac{\eta}{a}$.

Remark 2.1. Note that the symmetrization of G_0 appears naturally in Hamilton's equations of motion. For instance, consider formally Hamilton's equations $\dot{z} = \mathcal{J}\nabla H$, $\mathcal{J}$ the canonical form, with the quadratic Hamiltonian $H = \frac{1}{2} z^T E z$. Then Hamilton's equations are $\dot{z} = \frac{1}{2}(E + E^T)z$.

2.2. Spectral formulation and Galerkin truncations

As the Hamiltonians above involve pseudo-differential operators, it is natural to consider Fourier spatial discretizations.

Let $\eta(x,t)$ and $\xi(x,t)$ be 2π-periodic real functions, $\hat{\eta}_k$, $\hat{\xi}_k$, $k \in \mathbb{Z}$, their respective Fourier coefficients. Then Hamilton's equations become

$$\begin{cases} \partial_t \hat{\eta}_k = \dfrac{\partial H}{\partial \hat{\xi}_{-k}} \\ \partial_t \hat{\xi}_k = -\dfrac{\partial H}{\partial \hat{\eta}_{-k}}, \end{cases} \quad k \in \mathbb{Z}\ . \tag{2.27}$$

It is possible to assume $k \in \mathbb{Z} \setminus \{0\}$ in these equations, since $\hat{\eta}_0 = \hat{\xi}_0 = 0$ imply $\partial_t \hat{\eta}_0 = 0$, $\partial_t \hat{\xi}_0 = 0$. Thus $\hat{\eta}_0 = \hat{\xi}_0 = 0$ define an invariant subspace of (2.27).

Since η, ξ are real-valued functions, we also have $\hat{\eta}_{-k} = \hat{\eta}_k^*$ and $\hat{\xi}_{-k} = \hat{\xi}_k^*$. Then we can make the change of variables from $\{\hat{\eta}_k, \hat{\xi}_k \mid k \in \mathbb{Z} \setminus \{0\}\}$, to the variables $\{\hat{\eta}_k, \hat{\eta}_k^*, \hat{\xi}_k, \hat{\xi}_k^* \mid k \in \mathbb{Z}^+\}$, $\forall k \in \mathbb{Z}$, and write (2.27) as

$$\begin{cases} \partial_t \hat{\eta}_k = \dfrac{\partial H}{\partial \hat{\xi}_k^*} \\ \partial_t \hat{\xi}_k = -\dfrac{\partial H}{\partial \hat{\eta}_k^*}, \end{cases} \quad k \in \mathbb{Z}^+\ . \tag{2.28}$$

Galerkin truncations are obtained by considering

$$\begin{cases} \partial_t \hat{\eta}_k = \dfrac{\partial H}{\partial \hat{\xi}_k^*} \\ \partial_t \hat{\xi}_k = -\dfrac{\partial H}{\partial \hat{\eta}_k^*}, \end{cases} \quad k \in J_M, \ \text{ with } J_M = \{1, \ldots, M\}\ . \tag{2.29}$$

3. Spectral analysis for the operator $Sym(D\tanh(h(x)D))$

The main goal of this section is to present some numerical results on the spectral analysis of the linear part of the Dirichlet–Neumann operator of the model (2.25). We first present some general considerations leading to (2.25). The idea is to define an operator that has a relatively simple expression and satisfies some structural properties of the exact linear Dirichlet–Neumann operator. Specifically, one may define the model Dirichlet–Neumann operator, denoted by $\mathcal{A}_{G_0} = \text{Approximate}(G_0(\beta))$, that satisfies

i. $(\mathcal{A}_{G_0})[f](x)$ is real if f is real.
ii. $\mathcal{A}_{G_0}$ is a formally symmetric operator, that is $\langle f, \mathcal{A}_{G_0} g\rangle = \langle \mathcal{A}_{G_0} f, g\rangle$, where $\langle f, g\rangle = \int_{\mathbb{R}} f\, g\, dx$ is the standard L^2-inner product, $\langle f, g\rangle = \int_0^{2\pi} f\, g\, dx$ for 2π-periodic boundary conditions. f and g are in the domain of $\mathcal{A}_{G_0}$, see iii.
iii. The high frequency spectral asymptotics of $\mathcal{A}_{G_0}$ are those of the constant depth case. We make this more precise in the periodic case, requiring that the generalized dispersion relation $\omega_\kappa = \sqrt{\lambda_\kappa}$ v.s. κ, where the λ_κ is the κth eigenvalue of $\mathcal{A}_{G_0}$ in increasing order, approach the constant depth dispersion relation $\omega_\kappa = \sqrt{\kappa \tanh \kappa}$ as $k \longrightarrow \infty$. A similar convergence condition should apply to the eigenfunctions.
iv. $\mathcal{A}_{G_0}$ is a positive operator, that is $\langle f, \mathcal{A}_{G_0} f\rangle \geq c\|f\|^2$.

When $\beta = 0$ all properties (i)–(iv) are satisfied by $\mathcal{A}_{G_0} = D\tanh(h_0 D)$.

The simple generalization of this operator $\mathcal{A}_{G_0} = D\tanh(h(x)D)$ is not in general symmetric but can be symmetrized to satisfy (ii). Property (i) is verified below. Properties (iii) and (iv) are verified numerically below.

In the 2π-periodic framework we let $a(x, k)$ be 2π-periodic function in the variable x and define $a(x, D)$ as

$$a(x, D)[\xi](x) = \frac{1}{2\pi}\sum_{k=-\infty}^{\infty} a(x, k)\hat{\xi}_k e^{ikx}. \tag{3.1}$$

Also

$$a(x, k) = \sum_{\lambda\in\mathbb{Z}} e^{i\lambda x}\hat{a}_\lambda(k), \tag{3.2}$$

where $\hat{a}_\lambda(k)$ are the Fourier coefficients in the x variable

$$\hat{a}_\lambda(k) = \int_0^{2\pi} a(x, k)e^{-i\lambda x}\,dx, \quad \lambda \in \mathbb{Z}. \tag{3.3}$$

Then the quadratic form $K_{a(x,D)}$, defined as

$$K_{a(x,D)} = \frac{1}{2}\int_0^{2\pi} \xi\, a(x, D)\xi\, dx, \tag{3.4}$$

becomes

$$K_{a(x,D)} = \frac{1}{2}\int_0^{2\pi} \xi\, a(x, D)\xi dx = \frac{\pi}{2}\sum_{[k,\lambda]\in\mathbb{Z}^2} \hat{\xi}_{-k-\lambda}\hat{\xi}_k\hat{a}_\lambda(k) = \frac{\pi}{2}\sum_{[k,\lambda]\in\mathbb{Z}^2} \hat{\xi}_k\hat{\xi}_\lambda\hat{a}_{-k-\lambda}(\lambda). \tag{3.5}$$

Also, if ξ is real-valued then $[a(x, D)]\xi$ is also real-valued. Then $[a(x, D)]\xi = \overline{\alpha(x, D)\xi}$, and

$$a(x, \mu) = \overline{a(x, -\mu)}, \quad \forall x, \mu \in \mathbb{R} \tag{3.6}$$

$$\hat{a}_\lambda(k) = \overline{\hat{a}_\lambda(k)} = \hat{a}_\lambda(-k), \qquad \hat{a}_{-\lambda}(k) = \overline{\hat{a}_\lambda(-k)} = \overline{\hat{a}_\lambda(k)}, \quad \forall\lambda, k \in \mathbb{Z}. \tag{3.7}$$

It follows that, if $a(x, D)\xi$ is real, then the quadratic form $K_{Sym(a(x,D))}$ is

$$K_{Sym(a(x,D))} = \frac{1}{4\pi}\sum_{[k,\lambda]\in\mathbb{Z}^2} \hat{\xi}_k[\hat{a}_{\lambda-k}(k) + \overline{\hat{a}_{k-\lambda}(\lambda)}]\hat{\xi}^*_\lambda. \tag{3.8}$$

We also describe the Galerkin truncations of the quadratic forms obtained from $a(x, D)$ and its symmetrization. We will use real and imaginary parts to obtain real, symmetric bilinear forms. Let $\hat{\xi}^M = (\hat{\xi}_1, \ldots, \hat{\xi}_M)$ as in (2.29), and consider the Galerkin truncation $K^M_{a(x,D)}$ of $K_{a(x,D)}$,

$$\begin{aligned} K^M_{a(x,D)} &= \frac{1}{4\pi}\sum_{[k_1,k_2]\in J^2_M}\left[\hat{\xi}_{k_1}\hat{\xi}_{k_2}\hat{a}^*_{k_1+k_2}(k_2) + \hat{\xi}^*_{k_1}\hat{\xi}^*_{k_2}\hat{a}_{k_1+k_2}(k_2)\right] \\ &\quad + \frac{1}{4\pi}\sum_{[k_1,k_2]\in J^2_M}\left[\hat{\xi}_{k_1}\hat{\xi}^*_{k_2}\hat{a}_{-k_1+k_2}(k_2) + \hat{\xi}^*_{k_1}\hat{\xi}_{k_2}\hat{a}^*_{-k_1+k_2}(k_2)\right] \qquad (3.9) \\ &= \frac{1}{4\pi}((\hat{\xi}^M)^T, ((\hat{\xi}^M)^*)^T)\begin{pmatrix} P^* & S \\ S^* & P\end{pmatrix}\begin{pmatrix}\hat{\xi}^M \\ (\hat{\xi}^M)^*\end{pmatrix}, \qquad (3.10)\end{aligned}$$

with P, S defined implicitly by (3.9), (3.10). P^*, S^* are the complex conjugates of P, S respectively. To clarify what the matrix blocks P and S refer to, see Appendix B.

Letting $\hat{\xi}^M = \theta + i\zeta, \theta, \zeta \in \mathbb{R}^M$, we have

$$K^M_{a(x,D)} = \frac{1}{4\pi}(\theta^T, \zeta^T)\begin{pmatrix} Re(P^* + S^* + P + S) & -Im(P^* - S^* + S - P) \\ -Im(P^* + S^* - S - P) & -Re(P^* - S^* - S + P)\end{pmatrix}\begin{pmatrix}\theta \\ \zeta\end{pmatrix}.$$

Letting

$$\mathcal{M} = \frac{1}{4\pi}\begin{pmatrix} Re(P^* + S^* + P + S) & -Im(P^* - S^* + S - P) \\ -Im(P^* + S^* - S - P) & -Re(P^* - S^* - S + P)\end{pmatrix}, \tag{3.11}$$

and $\mathcal{M}_{Sym} = \frac{1}{2}(\mathcal{M} + \mathcal{M}^T)$, we then have

$$K^M_{Sym(a(x,D))} = \left(\theta^T, \zeta^T\right)\mathcal{M}_{Sym}\begin{pmatrix}\theta \\ \zeta\end{pmatrix}. \tag{3.12}$$

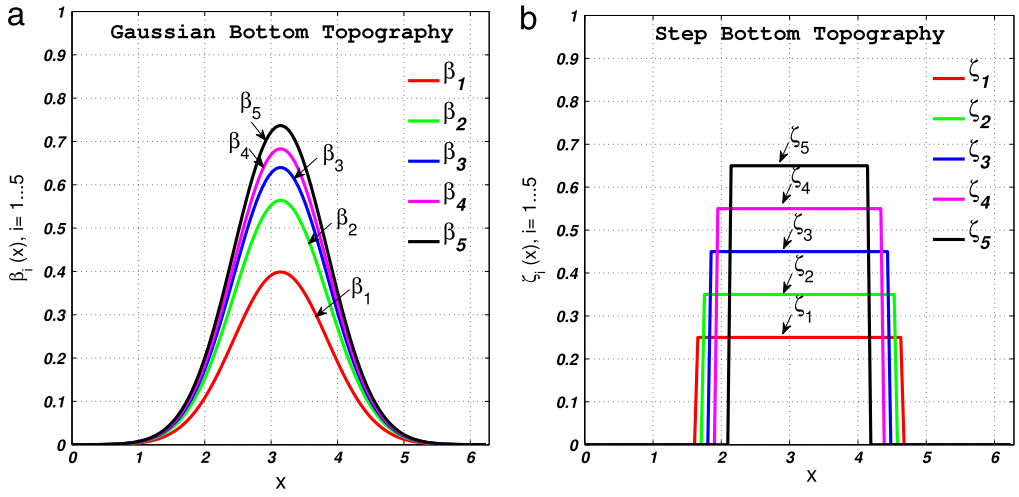

Fig. 1. (a) *Gaussian* family depth profile, and (b) *Step* family depth profile.

3.1. Numerical spectra of $Sym(D\tanh(h(x)D))$ for different depth profiles

We now study the linear system corresponding to the quadratic part $H_{2,Q}$ of the Hamiltonian H_2 of (2.26) with 2π-periodic boundary conditions. We have

$$H_{2,Q} = \frac{1}{2}\int_0^{2\pi} \left[\xi \left(Sym\left(D\tanh\left(\sqrt{\epsilon}h(x)D\right)\right)\right)\xi + \eta^2\right] dx. \tag{3.13}$$

The first term (the quadratic part of the kinetic energy) is of the form $K_{Sym(a(x,D))}$, with $Sym(a(x,D))$ the model Dirichlet–Neumann operator $\mathcal{A}_{G_0} = G_0(\beta)$. We have that every $\lambda \in \sigma(G_0(\beta))$ corresponds to a frequency $\omega(\lambda) = \sqrt{\lambda}$ of the linear system of (3.13).

In the numerical study below we use the Galerkin truncations above in the real formulation. The model Dirichlet–Neumann operator $\mathcal{A}_{G_0}$ is then represented by the matrix $\mathcal{M}_{Sym}$ of (3.12). We use

$$a(x,k) = \frac{1}{\sqrt{\epsilon}}\tanh\left(\sqrt{\epsilon}(1-\beta(x))k\right)k, \tag{3.14}$$

and the following depth profiles: the one-parameter *Gaussian* family

$$\beta(x) = \beta_i(x) = \frac{1}{\sqrt{a_i}}e^{-(x-\pi)^2}, \tag{3.15}$$

with $a_1 = 2\pi$, $a_2 = \pi$, $a_3 = \pi - 0.7$, $a_4 = \pi - 1$, $a_5 = \pi - 1.3$, see Fig. 1(a), and the *Step* family

$$\zeta_i(x) = \begin{cases} 0 & \text{for } 0 \le x < \pi - d_i, \\ b_i & \text{for } \pi - d_i \le x < \pi + d_i, \\ 0 & \text{for } \pi + d_i \le x \le 2\pi, \end{cases} \tag{3.16}$$

with $b_1 = 0.25$, $b_2 = 0.35$, $b_3 = 0.45$, $b_4 = 0.5$, $b_5 = 0.65$, and $d_1 = 1.5$, $d_2 = 1.4$, $d_3 = 1.3$, $d_4 = 1.2$, $d_5 = 1.5$, see Fig. 1(b).

Fig. 2(a) and (b) show a visual representation of the size of the entries of $\mathcal{M}_{Sym}$ for the β_5 and ζ_5 bottom profiles of the *Gaussian* and *Step* families respectively in gray intensity color scale. We have used $k_{Max} = 2^5$ positive modes. The matrix $\mathcal{M}_{Sym}$ for $\beta \equiv 0$ is diagonal. Since we consider the real and imaginary parts of every mode, M_{Sym} is $2M \times 2M$.

In Fig. 2(a) and (b) we see that for variable depth $\mathcal{M}_{Sym}$ is not diagonal. The larger entries are on the diagonal and the decay from the diagonal is related to the amplitude and smoothness of $\beta(x)$ of (3.15) and (3.16). As the depth β becomes flatter we recover the diagonal matrix seen for constant depth.

In Fig. 2(c) and (d) we show the matrices $\mathcal{M}_{sym}$ for the β_5 and ζ_5 profiles of *Gaussian* and *Step* families respectively with $k_{Max} = 2^9$. We see an enlargement around the diagonal that finishes in an skinny line, first the bright region "opens" and then "closes" around the diagonal for larger k. This suggests that the symbol of constant depth operator dominates the behavior for larger k. In other words, the high frequencies do not feel the bottom topography.

In Fig. 3 we show the generalized dispersion relation for different depths. We plot $\omega_\kappa = \sqrt{\lambda_\kappa}$ v.s. κ, where the λ_κ is the κth eigenvalue of $\mathcal{M}_{sym}(\beta)$. In each figure we also plot the constant depth dispersion relation $\omega_\kappa = \sqrt{\kappa\tanh\kappa}$. As β approaches the constant depth profile in each of the two families for the *Gaussian* family see Fig. 3(a) and for the *Step* family

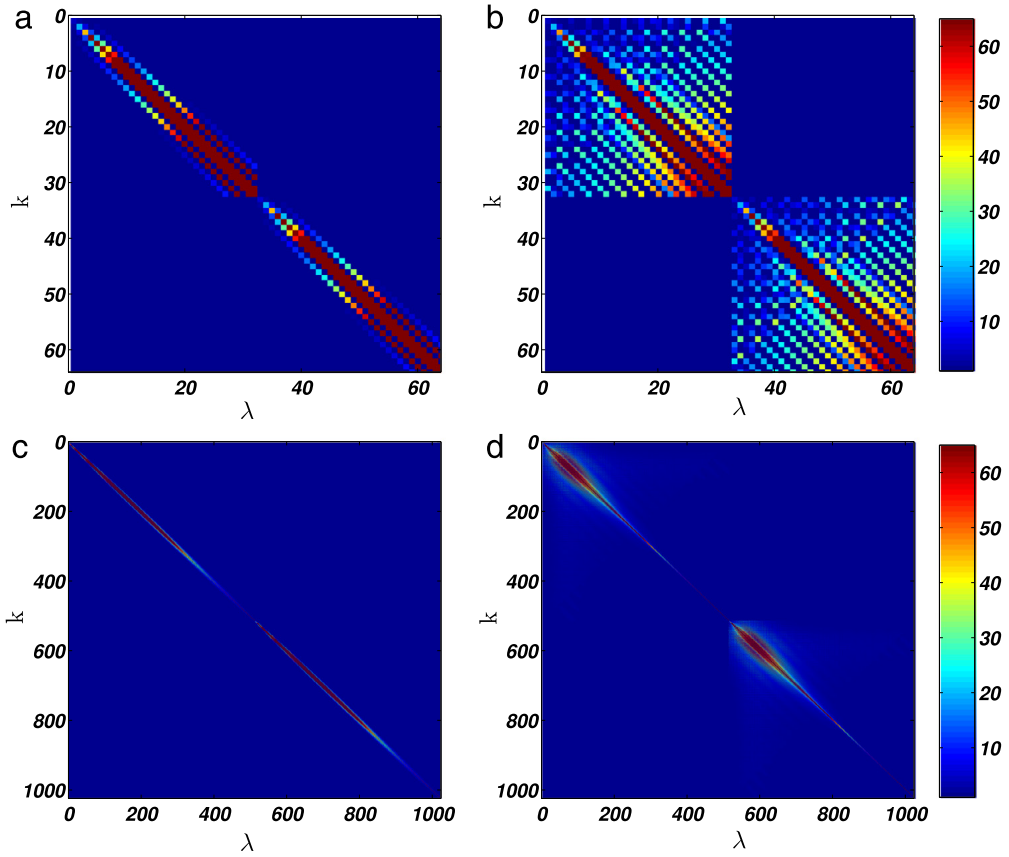

Fig. 2. Colormatrix representation of matrix $\mathcal{M}_{Sym}(\lambda, k)$. Figure (a) shows $\mathcal{M}_{Sym}(\beta_5)$ and (b) $\mathcal{M}_{Sym}(\zeta_5)$ with $k_{Max} = 2^5$. Figure (c) shows $\mathcal{M}_{Sym}(\beta_5)$ and (d) $\mathcal{M}_{Sym}(\zeta_5)$ with $k_{Max} = 2^9$, see (3.15), (3.16) for exact analytic expression of bottom profiles.

see Fig. 3(c) we see that the eigenvalues approach the constant depth dispersion relation in a monotonic way. Fig. 3(b), (d) also indicate that the ω_κ obtained for different depth profiles are much closer for large enough κ, i.e. for large enough κ we recover the constant depth dispersion.

We now indicate some effects of the topography on the eigenmodes of $\mathcal{M}_{Sym}$ for different bottom profiles. The main effects are:

A. *Steepening.* In Fig. 4 we plot the normal modes corresponding to the first three eigenvalues of $\mathcal{M}_{sym}$ for *Gaussian* topography β_5, see (3.15). Each eigenvalue λ_κ of $\mathcal{M}_{Sym}$ gives rise to two eigenmodes, one odd and one even. We also compare these eigenmodes to the constant depth eigenmodes, $\cos(\kappa x)$ and $\sin(\kappa x)$, $\kappa = 1, 2, 3 \ldots$.

In Fig. 5 we see the steepening of the first mode with increasing depth variation β_i of Fig. 1(a). The shapes are close but topography leads for steeper profiles. The steepening effect is observed for all lower to intermediate modes. Truncating with $k_{Max} = 2^6$, we calculated that for modes bigger than $\kappa = 37$ this effect is almost imperceptible.

B. *Modulation.* In Fig. 6 we show the amplitude modulation of the $\kappa = 15$ mode, using $k_{Max} = 2^7$. The range of wavelengths where this effect is clearly visible is roughly from $\kappa = 6$ to $\kappa = 30$. Using $k_{Max} = 2^6$, the effect is seen from $\kappa = 5$ to $\kappa = 18$. In both cases the effect is seen for lower to intermediate modes. This range is around the peak of the Fourier transform of β. High frequencies are not affected in this way by the bottom topography.

In Fig. 7 we see the Fourier amplitudes of the $\kappa = 1, 3, 5$, and 7 modes, corresponding to *Gaussian* profile β_5. As κ increases the bandwidth becomes smaller. For instance, the $\kappa = 1$ normal mode has a bandwidth of 17 modes, that is the amplitudes of all other modes are less or equal than 10^{-6} (using a truncation with $k_{Max} = 2^6$).

4. Numerical integration of the Whitham–Boussinesq model

In this section we integrate numerically the system derived from the Hamiltonian H_2, using the model Dirichlet–Neumann operator G_{Aprox_2} of (2.25). In the constant depth case H_2 reduces to H_0.

We examine two types of experiments, the separation of an initial disturbance into two counter-propagating waves, and the evolution of a Stokes wavetrain. We report first that in the constant depth case, the H_0 model seems to capture qualitatively results from the higher order model of Craig and Sulem [21]. In the variable depth case we see clear effects of the topography on the evolution of the wave crests, and a significant deformation of the Stokes wave.

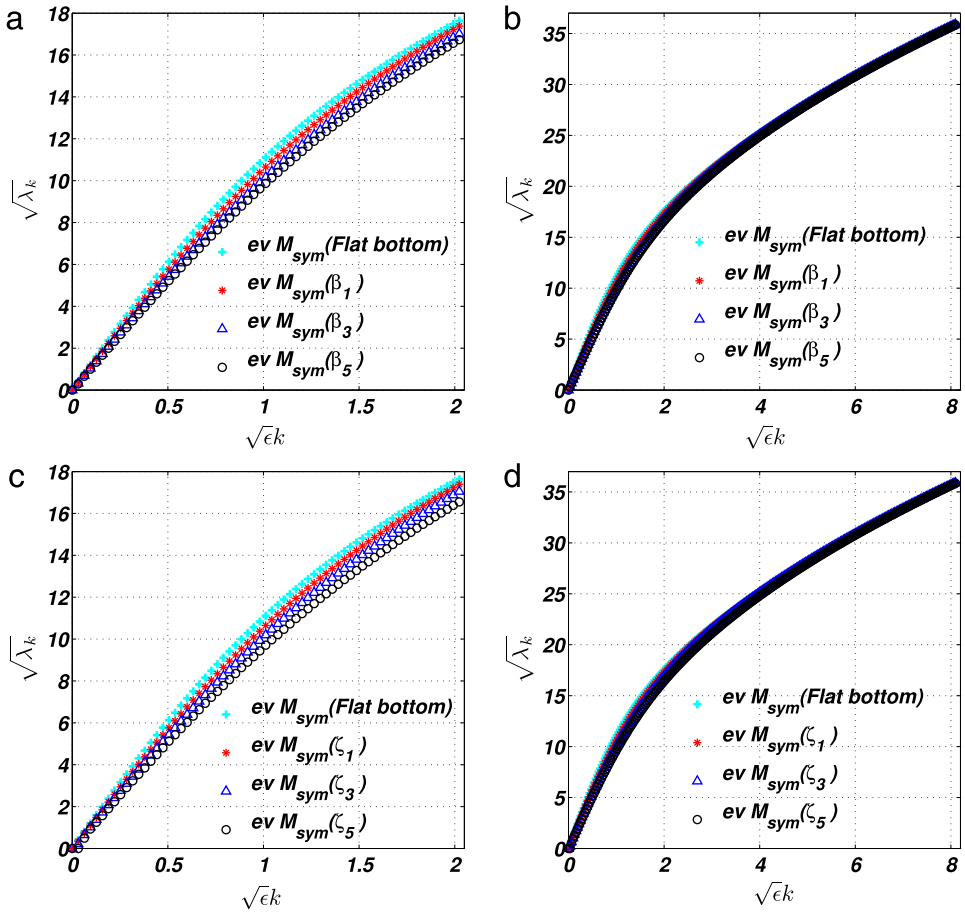

Fig. 3. *Generalized dispersion relation* for *Gaussian* and *Step* depth profiles compared with constant depth dispersion considering $\epsilon = 0.001$. For β_1, β_3, β_5, Figure (a) shows for $k_{\text{Max}} = 2^8$ and (b) shows for $k_{\text{Max}} = 2^{10}$. For ζ_1, ζ_3, ζ_5. Figure (c) shows for $k_{\text{Max}} = 2^8$ and (d) for $k_{\text{Max}} = 2^{10}$.

We discretize the system spatially using the spectral representations introduced in the previous sections. The Galerkin equations of motion are outlined in Appendix A. We comment on the possibility of a more efficient evaluation of the discretized system in Section 5. Numerical integration is performed using a fourth–fifth order Adams–Bashforth/Moulton (ABM) predictor–corrector scheme, see [22]. Some details are in Appendix A.

In all the numerical experiments below we consider smooth initial conditions η and ξ. We choose the time step Δt so that the relative error in the energy vs. t, $\frac{|E_t - E_0|}{E_0}$ is less than 10^{-3}. In the case of variable topography we have calibrated the accuracy of the integration using as initial conditions some of the normal modes computed in Section 3. The numerical scheme was implemented in MATLAB.

We first consider the propagation of a modulated wave packet, using the initial conditions of [21]

$$\eta_0(x) = 0.01 \quad e^{-\frac{4}{3}(x-\pi)^2}\cos(10x), \tag{4.1}$$

$$\xi_0(x) = 0, \quad \forall x \in [0, 2\pi]. \tag{4.2}$$

The depth is constant $h = 1$.

In Fig. 8 we show the evolution of the free surface, using the Hamiltonian flow of H_2. Specifically, in Fig. 8(c) we show $\eta(x, t)$ in the time interval from $t = 0$ to $t = 120$. We use time step $\Delta t = 0.0001$ and 2^5 Fourier modes. The nonlinearity parameter is $\epsilon = 0.01$ (note that ϵ also appears in the linear terms, this is due to the long-wave scaling).

Fig. 8(a) shows the wave profiles $\eta(x, t)$ at $t = 0$ and $t = 120$. We see the splitting of the initial wave profile into two waves traveling in opposite directions. After some time we observe the interference of the two packets due to the periodic boundary conditions. We observe the same qualitative behavior as in the numerical results presented in [21] by Craig and Sulem. The wave-crests in each wave packet have constant speeds. The evolution of the energy is indicated in Fig. 8(b). This quantity is conserved very well throughout the computation, with a relative error of $O(10^{-3})$ in the energy. The numerical scheme is seen to be slightly dissipative and we need to use a time step that is small enough to decrease the relative error in the energy.

Fig. 9 shows the evolution of the free surface $\eta(x, t)$ using H_2 and the initial conditions (4.1), (4.2), but now with variable depth β_5, see (3.15). The integration is from $t = 0$ to $t = 120$, and we use $k_{\text{Max}} = 2^5$, time step $\Delta t = 0.0001$, and $\epsilon = 0.01$.

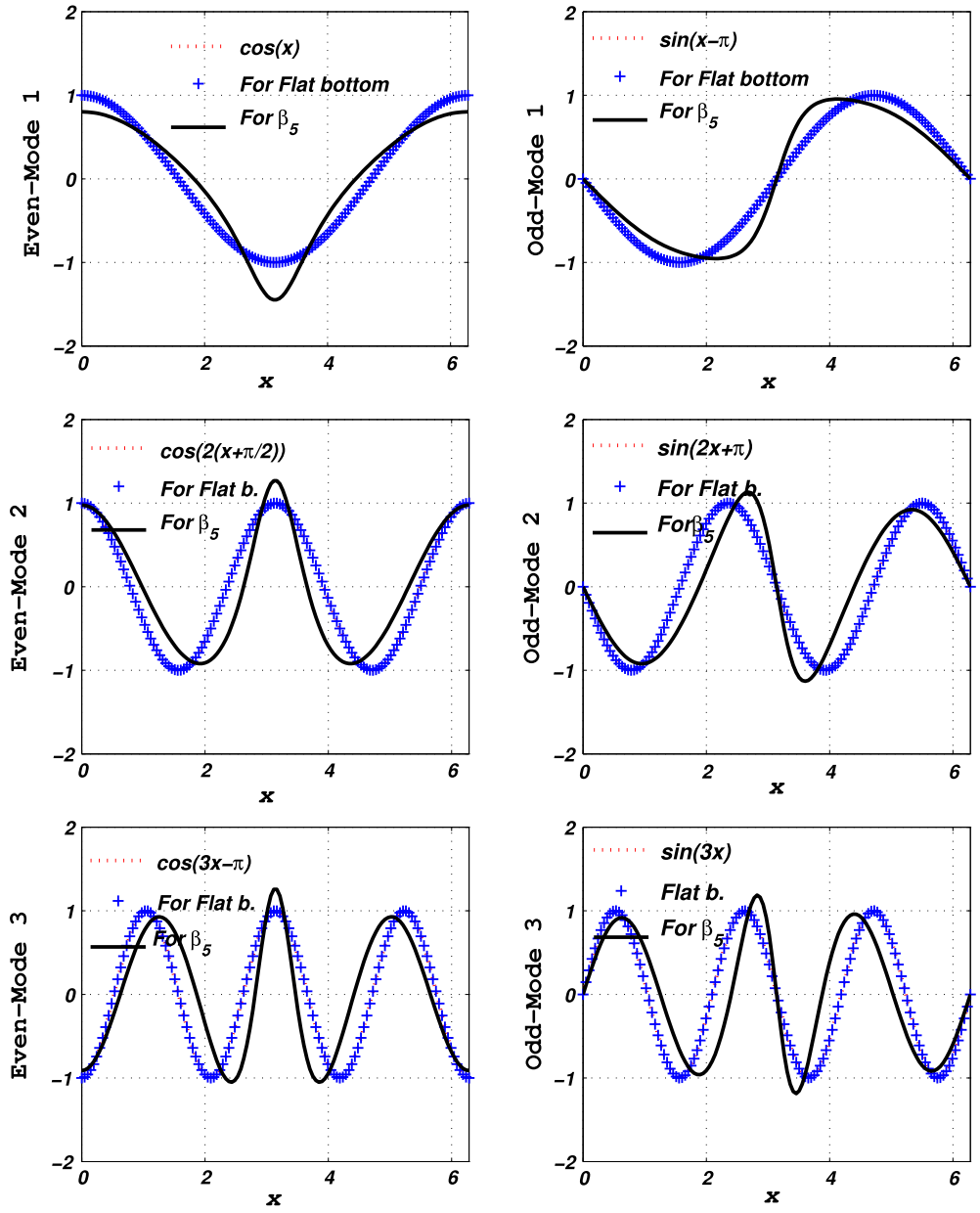

Fig. 4. The even and odd $\kappa = 1, 2$ and 3 eigenmodes for β_5 *Gaussian* bottom profile, see Fig. 1(a), with $k_{Max} = 2^6$ and $\epsilon = 0.001$.

Fig. 9(c) shows the free surface profile during the propagation through the variable depth channel. As in the constant depth case, we see the splitting of the initial wave profile into two wave-packets traveling in opposite directions, nevertheless in this case we observe that wave-crests have variable speed, and travel faster in the regions of higher depths.

The second numerical experiment uses as initial condition a second-order approximation of the Stokes wavetrain of the full Euler equations used in [21],

$$\eta_0(x) = a\cos(\lambda x) + \mu_2 a^2 \cos(2\lambda x), \tag{4.3}$$

$$\xi_0(x) = \nu_1 a \cosh(\lambda(\eta_0 + h))\sin(\lambda x) + \nu_2 a^2 \cosh(2\lambda(\eta_0 + h))\sin(2\lambda x), \tag{4.4}$$

where

$$\mu_2 = \frac{1}{2}\lambda\coth(h\lambda)\left(1 + \frac{3}{2\sinh(\lambda h)}\right), \qquad \nu_1 = \frac{\omega}{\lambda\sinh(h\lambda)}, \qquad \nu_2 = \frac{3}{8}\frac{3\omega}{\sinh^4(h\lambda)}, \tag{4.5}$$

and $a = 0.065$, $\lambda = 5$.

In Fig. 10 we show $\eta(x, t)$ using the equations for H_2 with constant depth $h = 1$. Specifically in Fig. 10(c), we plot $\eta(x, t)$ in the time interval from $t = 0$ to $t = 120$ in the (x, t)-plane with time step $\Delta t = 0.0001$. In Fig. 10(a) we show the initial

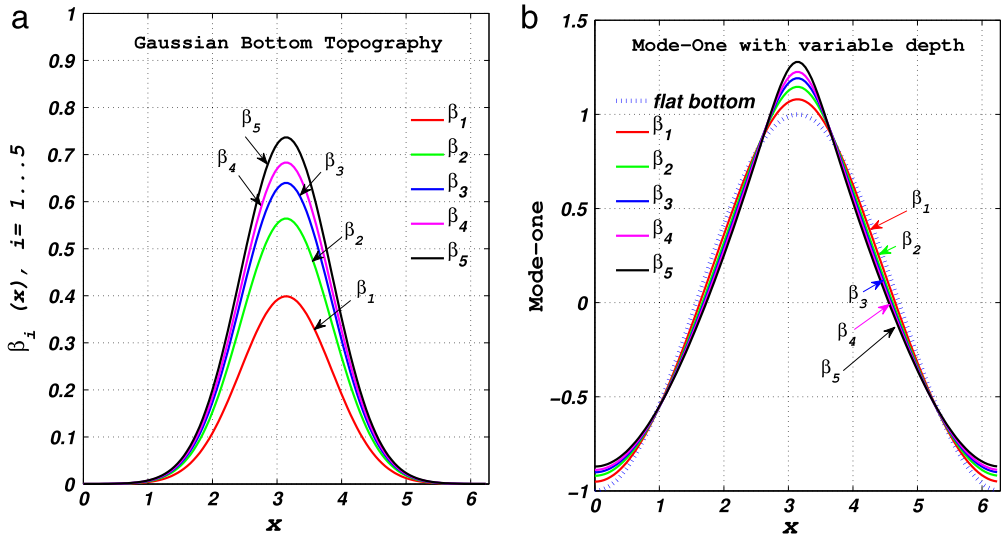

Fig. 5. Figure (b) shows the $\kappa = 1$ eigenmode for the *Gaussian* depth profiles of Figure (a), see Fig. 1(a).

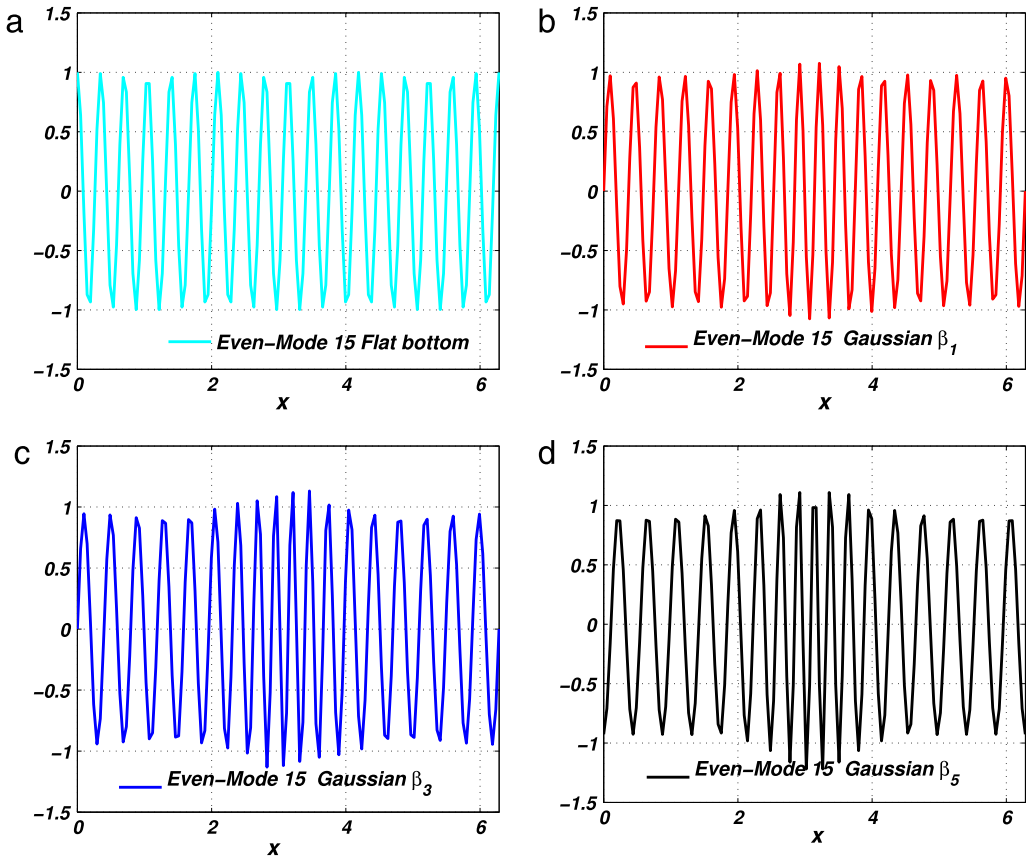

Fig. 6. Shows the $\kappa = 15$ eigenmode for the (a) Flat bottom profile (b) for the *Gaussian* bottom profile β_1, (c) for β_3 and (d) for β_5, from Eq. (3.15), see Fig. 1(a), with $k_{Max} = 2^6$, $\epsilon = 0.001$.

wave profile compared to the profile at $t = 120$. The computation was performed with a resolution of 2^5 Fourier modes, using $\epsilon = 0.065$ (this is also the value of the amplitude a of (4.3)). In Fig. 10(b) we indicate the conservation of energy. We observe the same qualitative behavior seen in the numerical results of [21] by Craig and Sulem. The wave amplitude stays near the traveling wave profile, with some oscillations in the width of the crests, as in [21].

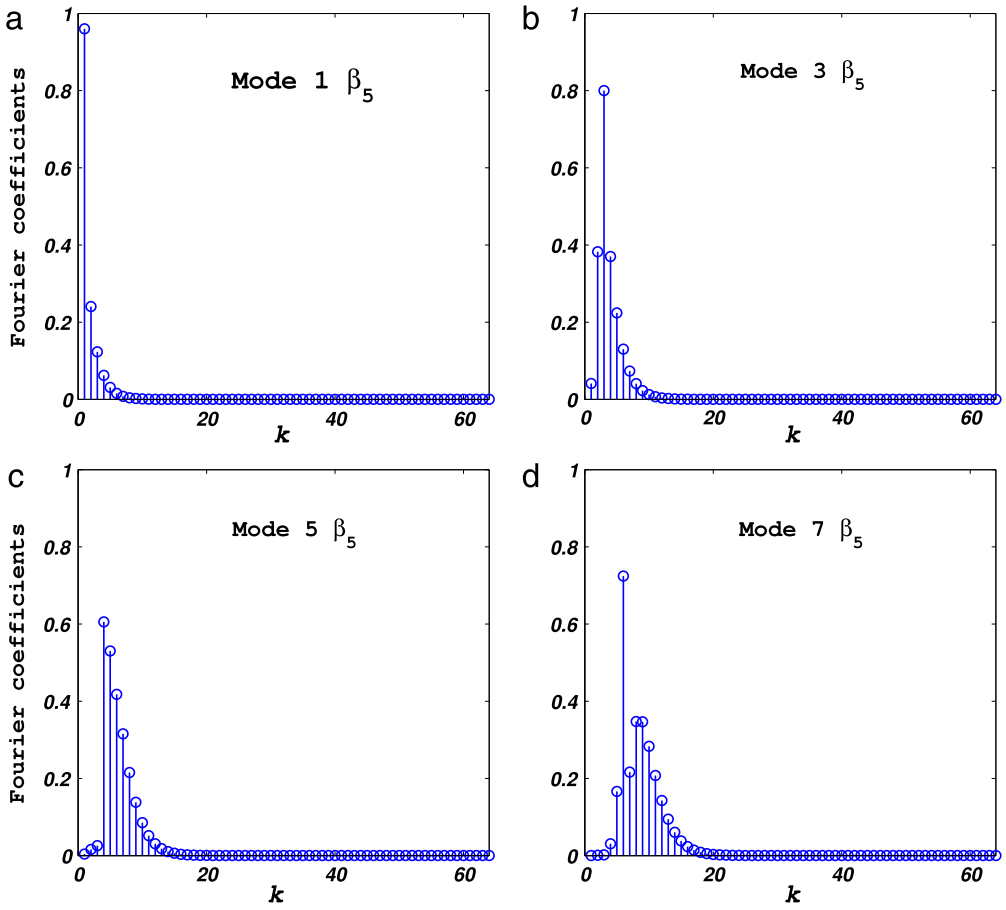

Fig. 7. Fourier spectrogram of $\kappa = 1, 3, 5$ and 7 eigenmodes for β_5 *Gaussian* profile, see Fig. 1(a), with $k_{Max} = 2^6$, $\epsilon = 0.001$.

Fig. 11 shows the evolution of the free surface $\eta(x, t)$ using H_2, the same initial condition given by (4.3), (4.4), but with variable depth β_5, as in (3.15). The time integration is from $t = 0$ to $t = 120$, and we use $k_{\text{Max}} = 2^5$, time step $\Delta t = 0.0001$, and $\epsilon = 0.065$.

Fig. 11(c) shows the free surface during as the Stokes wavetrain propagates through a channel with the variable *Gaussian* depth profile β_5 of (3.15). At the initial time the solution is a slightly perturbed Stokes wavetrain, and propagates as in Fig. 10(c). However, as time progresses and the wave starts to feel the bottom topography, it develops stronger deformations that start to destroy its shape. The deformation involves changes in the speed and height of some of the crests that roughly follow the topography.

We conclude with some remarks on the accuracy of the numerical integrations. The dependence of our results on the numerical time step Δt is indicated in Fig. 12, where we see that the wave profiles at time $t = 120$ obtained using time steps $\Delta t = 0.01$, $\Delta t = 0.001$, and $\Delta t = 0.0001$ are near. The relative energy error decreases notably as we decrease the time step. In Fig. 13 we indicate the dependence of the results on $k_{Max} = M$. Results obtained with $k_{Max} = 2^6$, $k_{Max} = 2^7$, and $k_{Max} = 2^8$ for depth profile β_5 are almost identical. Similar results were obtained for depth profile ζ_5. It then appears that $k_{Max} = 2^6$ gives reliable results, and that decreasing the time step could more important for increasing accuracy. (Computations with Δt of order 10^{-4}, $k_{Max} = 2^6$ were not possible because of storage limitations in our computer.)

5. Discussion

The proposed operator tanh $= Sym(Dtanh(h(x)D))$ offers a simple and compact approximation to the variable depth Dirichlet–Neumann operator $G_0(\beta)$. Our numerical simulations using the Whitham–Boussinesq model suggest that variable depth has significant effects on the dynamics of the long-wave model we considered. Also, the model is simple enough to motivate some further studies. For instance, [15] suggests the possibility of singularity formation at higher amplitudes, and the existence of solitons with a cusped profile. These are features introduced by the weaker dispersion, and can be studied in the presence of stronger depth effects that could not be captured by the system of H_1 in [15]. The new Whitham–Boussinesq model can be also used to study other effects of interest in nonlinear wave equations with spatial inhomogeneity, e.g. analogues of traveling waves. On the other hand, the relevance of our model to the water wave problem is tentative. This question requires comparisons with more detailed approximations to the full system.

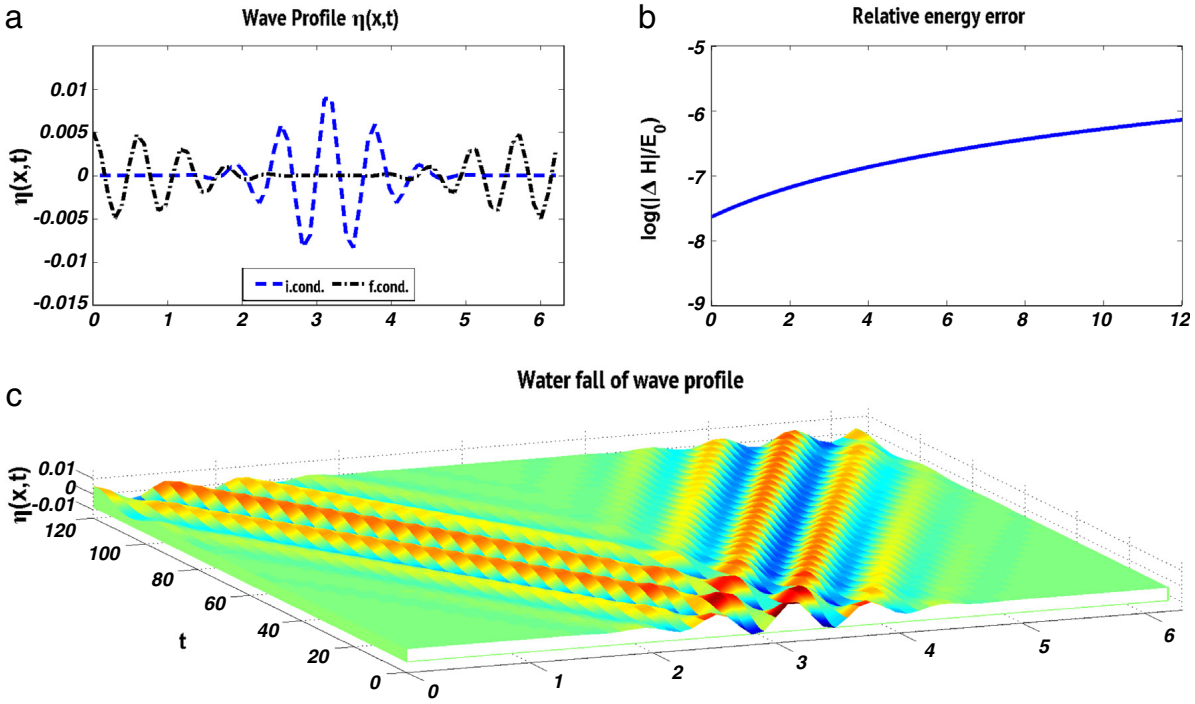

Fig. 8. (c) Evolution of the free surface $\eta_0(x,t) = 0.01\ e^{-\frac{4}{3}(x-\pi)^2}\cos(10x)$, $\xi_0(x) \equiv 0$, using H_2, with constant depth $h = 1.0$ (a) The dashed line shows the initial wave amplitude profile, the continuous line shows the wave amplitude profile at time $t = 120$. (b) The logarithm of the relative energy error from $t = 0$ to $t = 120$.

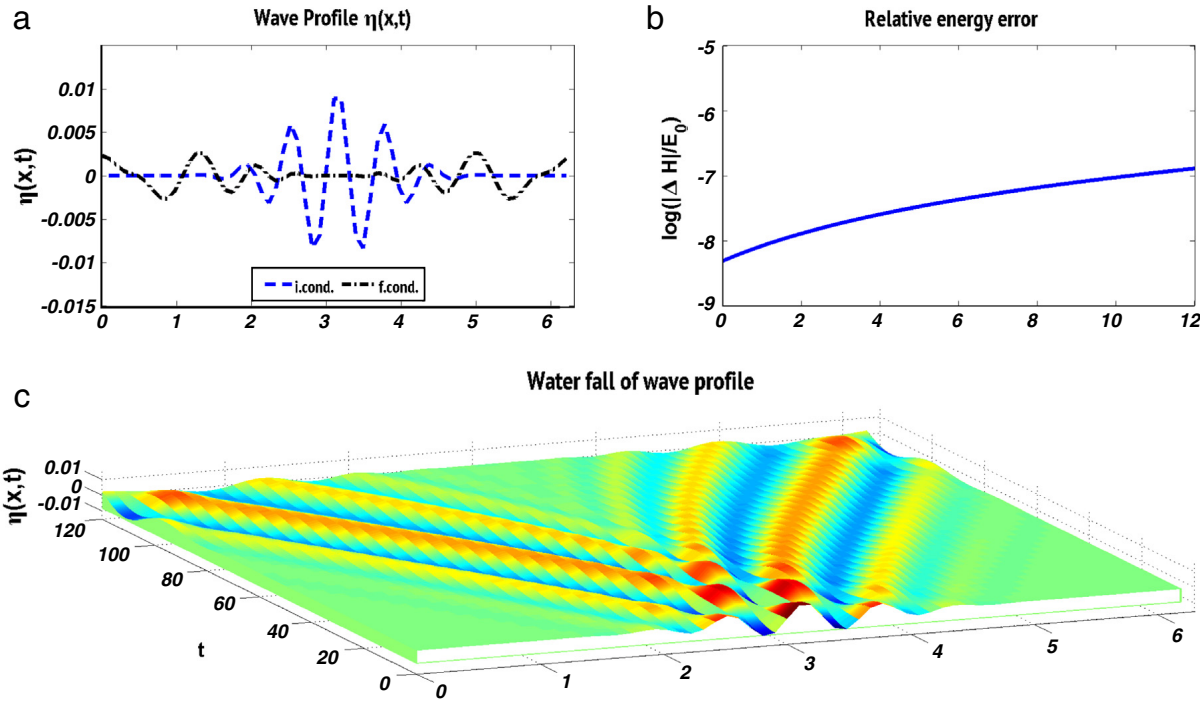

Fig. 9. (c) Evolution of the free surface $\eta_0(x,t) = 0,01e^{-\frac{4}{3}(x-\pi)^2}\cos(10x)$, $\xi_0(x) \equiv 0$, using H_2, and depth profile $\beta_5 = \frac{1}{\sqrt{\pi-1.3}}e^{-(x-\pi)^2}$ of Eq. (3.15). (a) The dashed line is the initial wave amplitude profile, the continuous line shows the wave amplitude profile at time $t = 120$. (b) The logarithm of the relative energy error from $t = 0$ to $t = 120$.

Another issue is the efficiency of the numerical evaluation of $\tanh = Sym(Dtanh(h(x)D))$. The present work did not emphasize efficiency, however the question becomes important in possible practical applications, for instance considering

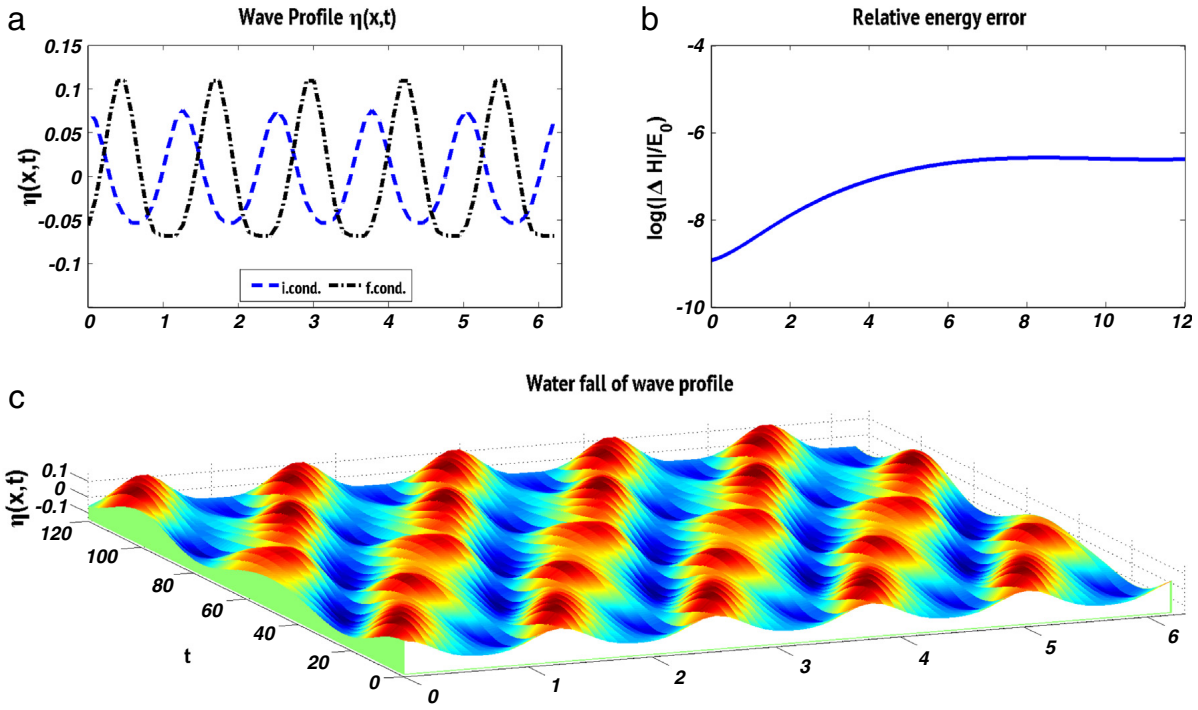

Fig. 10. (c) Evolution of the second-order approximation Stokes wavetrain using H_2, and $\lambda = 5$, $a = 0.065$, $h = 1.0$ (constant depth). (a) The dashed line shows the initial wave amplitude profile, the continuous line shows the wave amplitude at time $t = 120$. (b) The logarithm of the relative energy error from $t = 0$ to $t = 120$.

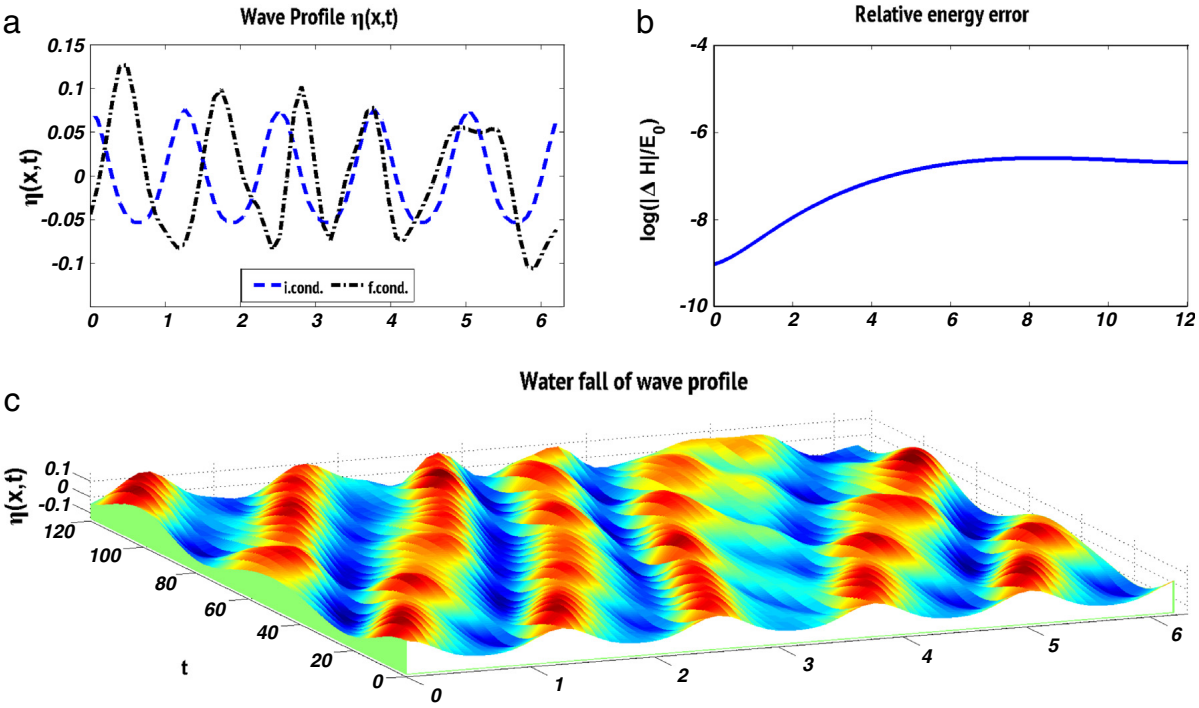

Fig. 11. (c) Evolution of the second-order approximation Stokes wavetrain using H_2, and $\lambda = 5$, $a = 0.065$, depth profile $\beta_5 = \frac{1}{\sqrt{\pi - 1.3}} e^{-(x-\pi)^2}$, see (3.15). (a) The dashed line shows the initial wave amplitude profile, the continuous line shows the wave amplitude profile at time $t = 120$. (b) The logarithm of the relative energy error from $t = 0$ to $t = 120$.

the three dimensional analogue of $\mathcal{A}_{G_0}$, with D replaced by $|D|$. By Section 3 and Appendix A, the evaluation of $\mathcal{A}_{G_0}$ in Fourier variables requires $O(M^2)$ operations, where M is the number of Fourier modes. The three dimensional analogue

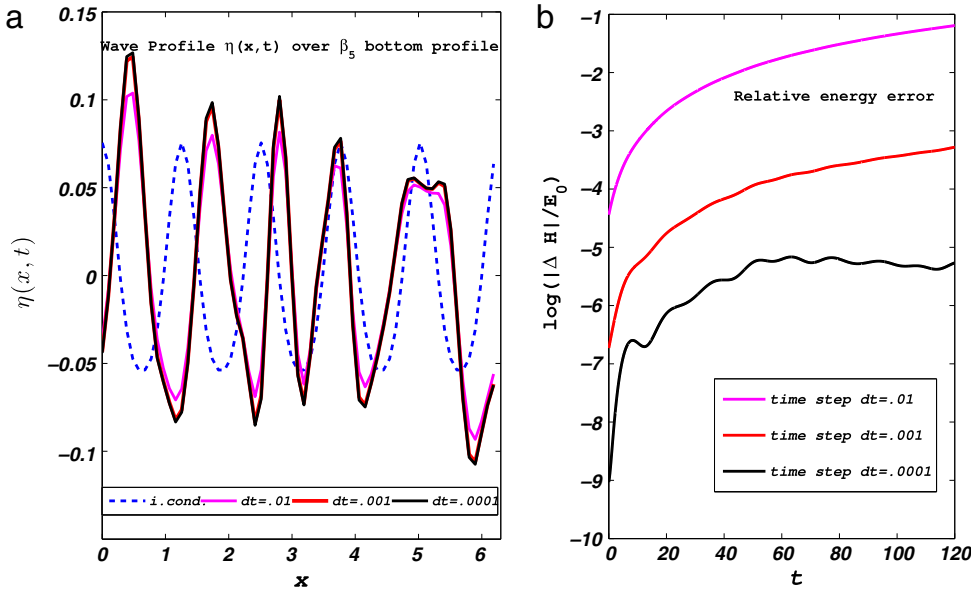

Fig. 12. (a) The dashed line shows the initial wave amplitude profile, the continuous lines in different colors show the wave amplitude at time $t = 120$, with $k_{Max} = 2^6$, and time steps $\Delta t = .01$ (magenta), $t = .001$ (red), $\Delta t = .0001$ (black). Figure (b) Shows the logarithm of the relative error from $t = 0$ to $t = 120$ for different time steps $\Delta t = .01$, $\Delta t = .001$, and $\Delta t = .0001$. (For interpretation of the references to color in this figure legend, the reader is referred to the web version of this article.)

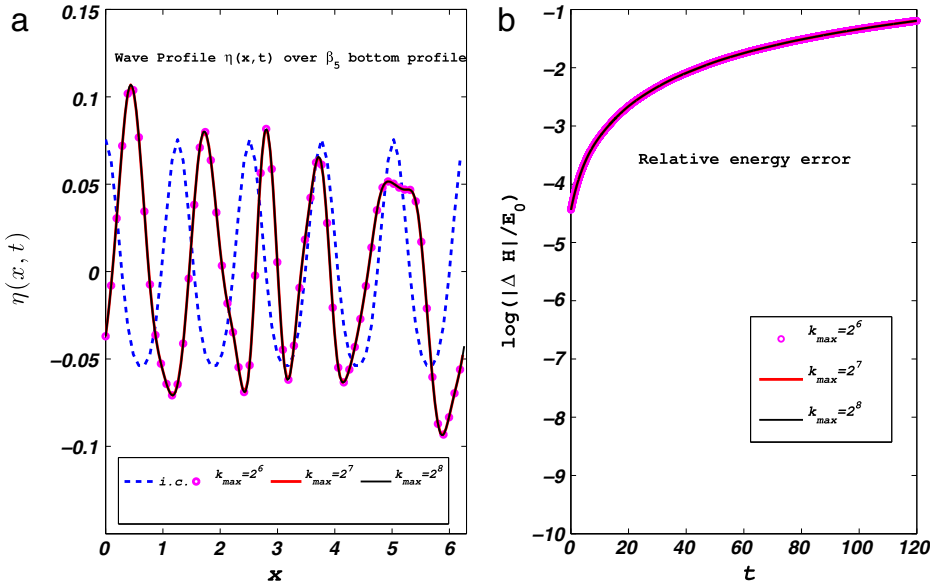

Fig. 13. (a) The dashed line shows the initial wave amplitude profile, the continuous line in different colors shows the wave amplitude at time $t = 120$ with time step $\Delta t = .01$ for $k_{Max} = 2^6$ (magenta), red $k_{Max} = 2^7$ (red), $k_{Max} = 2^8$ (black) Figure (b) Shows the logarithm of the relative error from $t = 0$ to $t = 120$ for $k_{Max} = 2^6, 2^7$, and 2^8. (For interpretation of the references to color in this figure legend, the reader is referred to the web version of this article.)

would require $O(M^4)$ operations. The cost is therefore comparable to the cost of evaluating the quadratic nonlinearity in spectral variables. The nonlinearity can be however evaluated with $O(M \log M)$ operations using the Fast Fourier transform (and $O(M^2 \log M)$ operations in three dimensions). The structure of $\mathcal{A}_{G_0}$ does not suggest any simplification in the nodal representation. We remark however that the plots of the spectral truncations $\mathcal{A}_{G_0}$, e.g. in Fig. 2, suggest that a full matrix multiplication may not be necessary, since the matrix decays rapidly away from the diagonal, especially for large wavenumbers. Thus a scheme where we use a banded matrix up to a certain wavelength, and a diagonal matrix for larger wavelengths may give satisfactory results. A banded structure would require at most $O(MR)$ and $O(M^2R)$ operations in two and three dimensions respectively, where R would be the width of the band. This would make the cost of the evaluation of $\mathcal{A}_{G_0}$ comparable to the cost of the pseudospectral method. The number R would depend on the depth variation β, e.g. its smoothness, and can be determined numerically.

Note that Guyenne and Nicholls approximate $G_0(\beta)$ in two and three dimensions using the expansion of $L(\beta)$ in powers of β, see [18], [19,14]. The terms L_j of this expansion only involve multiplications in space and in Fourier space, see e.g. (2.21) for L_1, and can be evaluated at a cost of $O(M \log M)$, $O(M^2 \log M)$ operations in two and three dimensions respectively. A possible drawback is the presence of higher derivatives in L_j as j is increased, and the authors also use high frequency truncations of the derivatives. The question of whether the particular $\mathcal{A}_{G_0}$ or other approximations of the Dirichlet–Neumann operator that avoid expansions in the depth variation can be evaluated with an efficiency that is comparable to that of pseudospectral methods seems to be an interesting problem for further study.

Acknowledgments

We would like to thank especially Professor Antonmaria Minzoni for his useful and enlightening discussions and for his endless encouragement and patience. Professor Minzoni made relevant suggestions and comments that have enriched the analysis and have helped our understanding of the Whitham–Boussinesq equation. He was also involved in the process of verifying the effectiveness and robustness of the numerical scheme. Rosa María Vargas-Magaña was supported by Conacyt PhD scholarship 213696. We also acknowledge partial support from grants SEP-Conacyt 177246 and PAPIIT IN103916.

Appendix A

We show the equations of motion derived from the Hamiltonians H_1, and H_2. The corresponding Galerkin approximations, see (2.29), are denoted by H_1^M, and H_2^M respectively.

Hamilton's equations for the Hamiltonian H_1^M are

$$\frac{\partial \hat{\eta}_k}{\partial t} = \frac{k}{\sqrt{\epsilon}} \tanh\left(\sqrt{\epsilon} k\right) \left(\frac{1}{2\pi} \hat{\xi}_k\right) + \frac{\epsilon}{4\pi^2} \sum_{k_1 \in J_M} \left(-k k_1 \hat{\xi}_{k_1} \hat{\beta}_{-k_1+k} + k k_1 \hat{\xi}^*_{k_1} \hat{\beta}_{k+k_1}\right) \tag{A.1}$$

$$+ \mathcal{N}_{1,k}(\hat{\eta}^M, (\hat{\eta}^M)^*, \hat{\xi}^M, (\hat{\xi}^M)^*), \tag{A.2}$$

$$\frac{\partial \hat{\xi}_k}{\partial t} = -\frac{1}{2\pi} \hat{\eta}_k + \mathcal{N}_{2,k}(\hat{\eta}^M, (\hat{\eta}^M)^*, \hat{\xi}^M, (\hat{\xi}^M)^*), \quad k = 1, \ldots, M. \tag{A.3}$$

The $\mathcal{N}_{i,k}(\hat{\eta}^M, (\hat{\eta}^M)^*, \hat{\xi}^M, (\hat{\xi}^M)^*)$ are the nonlinear terms calculated from (2.29). They are given by

$$\mathcal{N}_{1,k} = \begin{cases} -\dfrac{\epsilon}{4\pi^2} \left(\displaystyle\sum_{k_1=1}^{M-1} k_1 \hat{\xi}^*_{k_1} \hat{\eta}_{1+k_1} + \sum_{k_1=2}^{M} k_1 \hat{\xi}_{k_1} \hat{\eta}^*_{-1+k_1} \right), & k = 1, \\ \dfrac{\epsilon}{8\pi^2} \Big(-\displaystyle\sum_{k_1=1}^{M-k} k k_1 \hat{\xi}^*_{k_1} \hat{\eta}_{k+k_1} + \sum_{k_1=1}^{k-1} k_1 k \hat{\xi}_{k_1} \hat{\eta}_{k-k_1} \\ \qquad + \displaystyle\sum_{k_1=k+1}^{M} k k_1 \hat{\xi}_{k_1} \hat{\eta}^*_{-k+k_1} \Big), & k = 2, \ldots, M-1, \\ \dfrac{\epsilon M}{4\pi^2} \displaystyle\sum_{k_1=1}^{M-1} k_1 \hat{\xi}_{k_1} \hat{\eta}_{M-k_1}, & k = M, \end{cases} \tag{A.4}$$

$$\mathcal{N}_{2,k} = \begin{cases} \dfrac{\epsilon}{8\pi^2} \left(\displaystyle\sum_{k_2=1}^{M-1} k_2(1+k_2) \hat{\xi}^*_{k_2} \hat{\xi}_{1+k_2} + \sum_{k_2=2}^{M} k_2(-1+k_2) \hat{\xi}_{k_2} \hat{\xi}^*_{-1+k_2} \right), & k = 1, \\ \dfrac{\epsilon}{8\pi^2} \Big(-\displaystyle\sum_{k_2=1}^{k-1} k_2(k-k_2) \hat{\xi}_{k_2} \hat{\xi}_{k-k_2} + \sum_{k_2=1}^{M-k} k_2(k+k_2) \hat{\xi}^*_{k_2} \hat{\xi}_{k+k_2} \\ \qquad + \displaystyle\sum_{k_2=k+1}^{M} k_2(-k+k_2) \hat{\xi}_{k_2} \hat{\xi}^*_{-k+k_2} \Big), & k = 2, \ldots, M-1, \\ -\dfrac{\epsilon}{8\pi^2} \displaystyle\sum_{k_2=1}^{M-1} k_2(M-k_2) \hat{\xi}_{k_2} \hat{\xi}_{M-k_2}, & k = M, \end{cases} \tag{A.5}$$

with $\hat{\eta}^M = (\hat{\eta}_1, \ldots, \hat{\eta}_M)$, $(\hat{\eta}^M)^* = (\hat{\eta}^*_1, \ldots, \hat{\eta}^*_M)$, similarly for $\hat{\xi}^M$ and $(\hat{\xi}^M)^*$.

Hamilton's equations for H_2 differ from those for H_1^M in the linear part. The spectral representation of H_2^M in the real variables $\rho = Re(\hat{\eta}^M) = Re(\hat{\eta}_1, \ldots, \hat{\eta}_k, \ldots, \hat{\eta}_M)$, $\tau = Im(\hat{\eta}^M) = Im(\hat{\eta}_1, \ldots, \hat{\eta}_k, \ldots, \hat{\eta}_M)$, $\theta = Re(\hat{\xi}^M) = Re(\hat{\xi}_1, \ldots,$

$\hat{\xi}_k, \ldots, \hat{\xi}_M)$, $\zeta = Im(\hat{\xi}^M) = Im(\hat{\xi}_1, \ldots, \hat{\xi}_k, \ldots, \hat{\xi}_M)$, $k \in J_M$, yields the following system in $\mathbb{R}^{4M}$:

$$\begin{bmatrix} \dot{\rho} \\ \dot{\tau} \\ \dot{\theta} \\ \dot{\zeta} \end{bmatrix} = \begin{pmatrix} 0 & M_2 \\ -I & 0 \end{pmatrix} \begin{bmatrix} \rho \\ \tau \\ \theta \\ \zeta \end{bmatrix} + \mathcal{N}^{Real}(\rho, \tau, \theta, \zeta). \tag{A.6}$$

$\mathcal{N}^{Real}(\rho, \tau, \theta, \zeta)$ denotes the nonlinear terms, as in (A.4), (A.5), and

$$M_2 = \begin{pmatrix} Sym(C_{11}) & -\frac{1}{2} Im((P^*)^T - P^T + P^* - P) \\ -\frac{1}{2} Im((P^*)^T - P^T + P^* - P) & Sym(C_{22}) \end{pmatrix}, \tag{A.7}$$

with P, $C_{11} = Re(P^* + S^* + P + S)$, and $C_{22} = -Re(P^* - S^* - S + P)$ as in (3.11). Also, I denotes the $2M \times 2M$ identity. In this case Hamilton's equations for the Hamiltonian H_2^M are written in real variables.

The nonlinear terms in real variables are given by

$$\mathcal{N}_{1,k}^{Real} = \begin{cases} -\frac{\epsilon}{4\pi^2}\Big(\sum_{k_1=1}^{M-1} k_1\theta_{k_1}^*\rho_{1+k_1} + \theta_{k_1}^*\tau_{1+k_1} + \zeta_{k_1}^*\rho_{\eta\,1+k_1} + \zeta_{k_1}^*\tau_{1+k_1} \\ \quad + \sum_{k_1=2}^{M} k_1\theta_{k_1}\rho_{-1+k_1}^* + \theta_{k_1}\tau_{-1+k_1}^* + \zeta_{k_1}\rho_{-1+k_1}^* + \zeta_{k_1}\tau_{-1+k_1}^*\Big) \quad \text{for } k = 1 \\ \frac{\epsilon}{8\pi^2}\Big(-\sum_{k_1=1}^{M-k} kk_1(\theta_{k_1}^*\rho_{k+k_1} + \theta_{k_1}^*\tau_{k+k_1} + \zeta_{k_1}^*\rho_{k+k_1} + \zeta_{k_1}^*\tau_{k+k_1}) \\ \quad + \sum_{k_1=1}^{k-1} k_1k\theta_{k_1}\rho_{\eta\,k-k_1} + \theta_{k_1}\tau_{k-k_1} + \zeta_{k_1}\rho_{k-k_1} + \zeta_{k_1}\beta_{k-k_1} \\ \quad + \sum_{k_1=k+1}^{M} kk_1\theta_{k_1}\rho_{-k+k_1}^* + \theta_{k_1}\tau_{-k+k_1}^* \\ \quad + \zeta_{k_1}\rho_{-k+k_1}^* + \zeta_{k_1}\tau_{-k+k_1}^*\Big) \quad \text{for } k = 2, \ldots, M-1 \\ \frac{\epsilon M}{4\pi^2}\Big(\sum_{k_1=1}^{M-1} k_1\theta_{k_1}\rho_{M-k_1} + \theta_{k_1}\tau_{M-k_1} + \zeta_{k_1}\rho_{M-k_1} + \zeta_{k_1}\tau_{M-k_1}\Big) \quad \text{for } k = M \end{cases} \tag{A.8}$$

$$\mathcal{N}_{2,k}^{Real} = \begin{cases} \frac{\epsilon}{8\pi^2}\Big(\sum_{k_2=1}^{M-1} k_2(1+k_2)(\theta_{k_2}^*\theta_{1+k_2} + \theta_{k_2}^*\zeta_{1+k_2} + \zeta_{k_2}^*\theta_{1+k_2} + \zeta_{k_2}^*\zeta_{1+k_2}) \\ \quad + \sum_{k_2=2}^{M} k_2(-1+k_2)(\theta_{k_2}\theta_{-1+k_2}^* + \theta_{k_2}\zeta_{-1+k_2}^* + \zeta_{k_2}\theta_{-1+k_2}^* \\ \quad + \zeta_{k_2}\zeta_{-1+k_2}^*)\Big) \quad \text{for } k = 1 \\ \frac{\epsilon}{8\pi^2}\Big(-\sum_{k_2=1}^{k-1} k_2(k-k_2)(\theta_{k_2}\theta_{k-k_2} + \theta_{k_2}\zeta_{k-k_2} + \zeta_{k_2}\theta_{k-k_2} + \zeta_{k_2}\zeta_{\xi\,k-k_2}) \\ \quad + \sum_{k_2=1}^{M-k} k_2(k+k_2)(\theta_{k_2}^*\theta_{k+k2} + \theta_{k_2}^*\zeta_{k+k_2} + \zeta_{k_2}^*\theta_{k+k2} + \zeta_{k_2}^*\zeta_{k+k_2}) \\ \quad + \sum_{k_2=k+1}^{M} k_2(-k+k_2)(\theta_{k_2}\theta_{-k+k_2}^* + \theta_{k_2}\zeta_{-k+k_2}^* \\ \quad + \zeta_{k_2}\theta_{-k+k_2}^* + \zeta_{k_2}\zeta_{-k+k_2}^*)\Big), \quad \text{for } k = 2, \ldots, M-1 \\ -\frac{\epsilon}{8\pi^2}\Big(\sum_{k_2=1}^{M-1} k_2(M-k_2)(\theta_{k_2}\theta_{M-k_2} + \theta_{k_2}\delta_{M-k_2} + \zeta_{k_2}\theta_{M-k_2} + \zeta_{k_2}\zeta_{M-k_2})\Big) \\ \quad \text{for } k = M. \end{cases} \tag{A.9}$$

To integrate the system of ODE (A.6) for $y = (\rho, \tau, \theta, \zeta) \in \mathbb{R}^{4M}$ we use a fourth–fifth order Adams–Bashforth/Moulton (ABM) predictor–corrector time integration scheme, initiated by a 4-stage Runge–Kutta scheme, see [22]. Accordingly, the predictor is defined as

$$y_{n+1} = y_n + \frac{\Delta t}{24}(55\dot{y}_n - 59\dot{y}_{n-1} + 37\dot{y}_{n-2} - 9\dot{y}_{n-3}),$$

and the corrector is

$$y_{n+1} = y_n + \frac{\Delta t}{720}(251\dot{y}_{n+1} + 646\dot{y}_n - 264\dot{y}_{n-1} + 106\dot{y}_{n-2} - 19\dot{y}_{n-3}).$$

Appendix B

Let $\hat{\xi}^M = (\hat{\xi}_1, \ldots, \hat{\xi}_M)$ as in (2.29), and consider the Galerkin truncation $K^M_{a(x,D)}$ of $K_{a(x,D)}$, assuming $\xi_0 = 0$. Moreover by remarks (3.6) and (3.7) we also assume $\hat{a}_{-\lambda}(k) = \hat{a}^*_\lambda(k)$ and $\hat{a}_\mu(-k) = \hat{a}_\mu(k)$ to obtain Eq. (3.9).

From the second summation of Eq. (3.9)

$$\sum_{[k_1,k_2]\in J^2_M} \hat{\xi}^*_{k_1}\hat{\xi}^*_{k_2}\hat{a}_{k_1+k_2}(k_2) \tag{B.1}$$

we obtain the matrix P as

$$P = \begin{pmatrix} \hat{a}_{1+1}(1) & \hat{a}_{1+2}(2) & \cdots & \hat{a}_{1+(M-2)}(M-2) & \hat{a}_{1+(M-1)}(M-1) & 0 \\ \hat{a}_{2+1}(1) & \hat{a}_{2+2}(2) & \cdots & \hat{a}_{2+(M-2)}(M-2) & 0 & 0 \\ \cdots & \cdots & \cdots & \cdots & \cdots & \cdots \\ \hat{a}_{(M-2)+1}(1) & \hat{a}_{(M-2)+2}(2) & 0 & 0 & 0 & 0 \\ \hat{a}_{(M-1)+1}(1) & 0 & \cdots & 0 & 0 & 0 \\ 0 & 0 & 0 & 0 & 0 & 0 \end{pmatrix}.$$

From the third summation of (3.9)

$$\sum_{[k_1,k_2]\in J^2_M} \hat{\xi}_{k_1}\hat{\xi}^*_{k_2}\hat{a}_{-k_1+k_2}(k_2) \tag{B.2}$$

we obtain the matrix S as

$$S = \begin{pmatrix} \hat{a}_{-1+1}(1) & \hat{a}_{-1+2}(2) & \cdots & \hat{a}_{-1+(M-1)}(M-1) & \hat{a}_{-1+M}(M) \\ \hat{a}_{-2+1}(1) & \hat{a}_{-2+2}(2) & \cdots & \hat{a}_{-2+(M-1)}(M-1) & \hat{a}_{-2+M}(M) \\ \cdots & \cdots & \cdots & \cdots & \cdots \\ \hat{a}_{-M+1}(1) & \hat{a}_{-M+2}(2) & \cdots & \hat{a}_{-M+(M-1)}(M-1) & \hat{a}_{-M+M}(M) \end{pmatrix}$$

$$= \begin{pmatrix} \hat{a}_0(1) & \hat{a}_1(2) & \cdots & \hat{a}_{M-2}(M-1) & \hat{a}_{M-1}(M) \\ \hat{a}^*_1(1) & \hat{a}_0(2) & \cdots & \hat{a}_{M-3}(M-1) & \hat{a}_{M-2}(M) \\ \cdots & \cdots & \cdots & \cdots & \cdots \\ \hat{a}^*_{M-1}(1) & \hat{a}^*_{M-2}(2) & \cdots & \hat{a}^*_1(M-1) & \hat{a}_0(M) \end{pmatrix}.$$

References

[1] R.S. Johnson, On the development of a solitary wave moving over an uneven bottom, in: Mathematical Proceedings of the Cambridge Philosophical Society, Vol. 73, Cambridge Univ Press, 1973, pp. 183–203.
[2] Gerald Beresford Whitham, Linear and Nonlinear Waves, Vol. 42, John Wiley & Sons, 2011.
[3] John W. Miles, On the Korteweg-de-Vries equation for a gradually varying channel, J. Fluid Mech. 91 (01) (1979) 181–190.
[4] A. Nachbin, G.C. Papanicolaou, Water waves inshallow channels of rapidly varying depth, J. Fluid Mech. 241 (1992) 311–332.
[5] E. Van Groesen, S.R. Pudjaprasetya, Uni-directional waves over slowly varying bottom. Part I: Derivation of kdv-type of equation, Wave Motion 18 (4) (1993) 345–370.
[6] Sung B. Yoon, Philip L.-F. Liu, A note on hamiltonian for long water waves in varying depth, Wave Motion 20 (4) (1994) 359–370.
[7] James T. Kirby, Nonlinear, dispersive long waves in water of variable depth. Technical report, DTIC Document, 1996.
[8] Bengt Fornberg, A numerical method for conformal mapping, SIAM J. Sci. Stat. Comput. 1 (3) (1980) 386–400.
[9] J.W. Dold, An efficient surface-integral algorithm applied to unsteady gravity waves, J. Comput. Phys. 103 (1992) 90–115.
[10] Vladimir E. Zakharov, Stability of periodic waves of finite amplitude on the surface of a deep fluid, J. Appl. Mech. Tech. Phys. 9 (2) (1968) 190–194.
[11] A.C. Radder, An explicit Hamiltonian formulation of surface waves in water of finite depth, J. Fluid Mech. 237 (1992) 435–455.
[12] John W. Miles, On Hamilton's principle for surface waves, J. Fluid Mech. 83 (01) (1977) 153–158.
[13] Walter Craig, Mark D. Groves, Hamiltonian long-wave approximations of the water-wave problem, Wave Motion 19 (4) (1994) 376–389.
[14] Walter Craig, Philippe Guyenne, David P Nicholls, Catherine Sulem, Hamiltonian long-wave expansions for water waves over a rough bottom, in: Proceedings of the Royal Society of London A: Mathematical,Physical and Engineering Sciences, Vol. 461, The Royal Society, 2005, pp. 839–887.
[15] Pedro Aceves-Sánchez, Antonmaria Minzoni, Panayotis Panayotaros, Numerical study of a nonlocal model for water-waves with variable depth, Wave Motion 50 (1) (2013) 80–93.
[16] Vladimir E. Zakharov, Weakly nonlinear waves on the surface of an ideal finite depth fluid, Amer. Math. Soc. Transl. (1998) 167–197.

[17] Daulet Moldabayev, Henrik Kalisch, Denys Dutykh, The Whitham equation as a model for surface water waves, Physica D 309 (2014) 99–107.
[18] Philippe Guyenne, David P Nicholls, Numerical simulations of solitary waves on plane slopes, Math. Comput. Simulation 69 (3) (2005) 269–281.
[19] Philippe Guyenne, David P Nicholls, A high-order spectral method for nonlinear water waves over moving bottom topography, SIAM J. Sci. Comput. 30 (1) (2007) 81–101.
[20] Maïté Gouin, Guillaume Ducrozet and Pierre Ferrant, Development and validation of a highly nonlinear model for wave propagation over a variable bathymetry, in: ASME 2015 34th International Conference on Ocean, Offshore and Artic Engineering, American Society of Mechanical Engineers, 2015, pp. 41213–41223.
[21] Walter Craig, Catherine Sulem, Numerical simulation of gravity waves, J. Comput. Phys. 108 (1) (1993) 73–83.
[22] William J.D. Bateman, Chris Swan, Paul H. Taylor, On the efficient numerical simulation of directionally spread surface water waves, J. Comput. Phys. 174 (1) (2001) 277–305.